


## Quantum simulations with nuclear magnetic resonance system

Chudan Qiu(邱楚丹), Xinfang Nie(聂新芳), and Dawei Lu(鲁大为)
**Citation:**Chin. Phys. B, 2021, 30 (**4**): 048201. DOI: 10.1088/1674-1056/abe299
Journal homepage: http://cpb.iphy.ac.cn; http://iopscience.iop.org/cpb

**What follows is a list of articles you may be interested in**

---

## Quantum annealing for semi-supervised learning

Yu-Lin Zheng(郑玉鳞), Wen Zhang(张文), Cheng Zhou(周诚), and Wei Geng(耿巍)
Chin. Phys. B, 2021, 30 (**4**): 040306. DOI: 10.1088/1674-1056/abe298

## Efficient self-testing system for quantum computations based on permutations

Shuquan Ma(马树泉), Changhua Zhu(朱畅华), Min Nie(聂敏), and Dongxiao Quan(权东晓)
Chin. Phys. B, 2021, 30 (**4**): 040305. DOI: 10.1088/1674-1056/abe29a

## Realization of arbitrary two-qubit quantum gates based on chiral Majorana fermions

Qing Yan(闫青) and Qing-Feng Sun(孙庆丰)
Chin. Phys. B, 2021, 30 (**4**): 040303. DOI: 10.1088/1674-1056/abe296

## Monitoring the formation of oil-water emulsions with a fast spatially resolved NMR spectroscopy method

Meng-Ting You(游梦婷), Zhi-Liang Wei(韦芝良), Jian Yang(杨健), Xiao-Hong Cui(崔晓红), Zhong Chen(陈忠)
Chin. Phys. B, 2018, 27 (**2**): 028201. DOI: 10.1088/1674-1056/27/2/028201

## Interfacial transport in lithium-ion conductors

Shaofei Wang(王少飞) and Liquan Chen(陈立泉)
Chin. Phys. B, 2016, 25 (**1**): 018202. DOI: 10.1088/1674-1056/25/1/018202

---

TOPICAL REVIEW — Quantum computation and quantum simulation

# Quantum simulations with nuclear magnetic resonance system*

Chudan Qiu(邱楚丹)[1], Xinfang Nie(聂新芳)[1,†], and Dawei Lu(鲁大为)[1,2,‡]

[1] Shenzhen Institute for Quantum Science and Engineering and Department of Physics, Southern University of Science and Technology, Shenzhen 518055, China

[2] Guangdong Provincial Key Laboratory of Quantum Science and Engineering, Southern University of Science and Technology, Shenzhen 518055, China

(Received 13 October 2020; revised manuscript received 4 January 2021; accepted manuscript online 3 February 2021)

Thanks to the quantum simulation, more and more problems in quantum mechanics which were previously inaccessible are now open to us. Capitalizing on the state-of-the-art techniques on quantum coherent control developed in past few decades, e.g., the high-precision quantum gate manipulating, the time-reversal harnessing, the high-fidelity state preparation and tomography, the nuclear magnetic resonance (NMR) system offers a unique platform for quantum simulation of many-body physics and high-energy physics. Here, we review the recent experimental progress and discuss the prospects for quantum simulation realized on NMR systems.

**Keywords:** nuclear magnetic resonance, quantum simulation, quantum phase transition, quantum gravity

**PACS:** 82.56.−b, 03.67.Lx, 05.30.Rt, 04.60.−m **DOI:** 10.1088/1674-1056/abe299

## 1. Introduction

In order to predict the evolution of a quantum system, numerical analysis is a traditional but demanding approach. Especially due to the exponential size of Hilbert space as a function of quantum subsystems, the limited number of subsystems for numerical analysis is a major obstacle to addressing quantum problems with desirable accuracy on a classical computer. Conversely, in many cases, the quantum simulation may offer a faster solution with a probably more illustrative perspective. More importantly, the qubits in quantum simulators are intrinsically able to store exponentially large amounts of information compared to classical bits. Furthermore, in recent years, quantum effects play an increasingly substantial role in modern technology, which leads to the new needs for quantum simulation. Meanwhile, the physical platforms, as well as the technologies required, have matured enough to enable the practical implementations, including superconducting circuits,[1,2] trapped ions,[3,4] neutral atoms,[5–7] photons,[8,9] spin-based systems such as impurity spins in solids[10,11] and nuclear magnetic resonance (NMR).

Among various candidates, nuclear spins manipulated using NMR are usually considered to be competent in small-scale quantum simulations.[12] Twenty years ago, many leading experiments blazed a trail in implementing complex multi-qubit gate operations using NMR.[13–15] In the following decades, more sophisticated techniques have been well developed in terms of endeavouring to simulate the dynamics of quantum systems.[16,17] More recently, the state-of-the-art 12-qubit coherent control has been demonstrated.[18,19]

These experimental advances in controlling spins promise the applications in disparate areas, including many-body physics and quantum gravity. Some problems in the former are formidably hard to tackle with classical computers due to the complexity arisen from the interactions between many quantum individuals. And the quantum gravity which aims at unifying quantum mechanics and Einstein gravity is a fundamental area but with many ideas remaining unveiled experimentally.

In this review, we present some representative experimental demonstrations in many-body systems and quantum gravity realized with NMR. First, we start with an introduction of NMR fundamentals in Section 2. Next, centered around a key quantity called out-of-time correlator (OTOC), the following Section 3 expounds on three topics where the OTOC serves as an excellent probe: (1) OTOC can differentiate the integrable and non-integrable systems and quantify the butterfly velocity in quantum chaos (Subsection 3.1); (2) OTOC can observe different signatures of many-body localization (MBL) and Anderson localization (AL), as an alternative metric instead of the entanglement entropy (Subsection 3.2); (3) OTOC can detect the dynamical quantum phase transition (DQPT) and mark the critical point in equilibrium dynamical phase transition (EQPT) between the paramagnetic and ferromag-

*Project supported by the National Key Research and Development Program of China (Grant No. 2019YFA0308100), the National Natural Science Foundation of China (Grant Nos. 12075110, 11905099, 11605005, 11875159, and U1801661), Guangdong Basic and Applied Basic Research Foundation, China (Grant No. 2019A1515011383), Science, Technology and Innovation Commission of Shenzhen Municipality (Grant Nos. ZDSYS20170303165926217, JCYJ20170412152620376, and JCYJ20180302174036418), and Guangdong Innovative and Entrepreneurial Research Team Program, China (Grant No. 2016ZT06D348).

†Corresponding author. E-mail: niexf@sustech.edu.cn

‡Corresponding author. E-mail: ludw@sustech.edu.cn

© 2021 Chinese Physical Society and IOP Publishing Ltd 

netic phases, surpassing the autocorrelation and the two-body correlation function as regards to the precision and robustness (Subsection 3.3). These results shed light on the underlying connections among quantum chaos, thermalization, and quantum gravity. Accordingly, based on Ryu–Takayanagi (RT) entropy, the profound relation between OTOC and anti-de Sitter/conformal field theory (Ads/CFT) duality directs us to Subsection 4.1. The experiment that RT entropy has been verified on perfect tensor state is elaborated. While the perfect tensors are viewed as the building blocks of the tensor network, this verification makes the first step toward studying quantum gravity experimentally. In the other Subsection 4.2, the successful simulations of geometry properties and local dynamics of quantum spacetime, with respect to quantum tetrahedrons and spinfoam vertex amplitude, respectively, open up an avenue studying loop quantum gravity (LQG). Finally, the challenges and prospects of quantum simulation with NMR are discussed in Section 5.

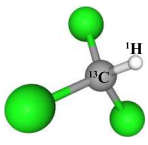
## 2. Basics of NMR

The well-defined qubits are represented by nuclear spins. Taking the spin-1/2 particle as an instance, the two levels with $\pm 1$ eigenvalues of $\hat{\sigma}_z$ respectively amount to two states of a qubit $|0\rangle$ and $|1\rangle$. These states are referred to as the computational basis states, based on which the wavefunctions are encoded. There are natural qubits like $^1$H, $^{13}$C, and $^{19}$F nuclear spins (see Fig. 1).

In the remainder of this article, we will restrict ourselves to the more comprehensible liquid-state NMR. In the liquid solution, where the rapid tumbling averages out the dipole–dipole interactions, the Hamiltonian with spin–spin interactions under the weak coupling approximation reads as ($\hbar = 1$)

$$\hat{H}_{\mathrm{NMR}} = -\sum_i \frac{\omega_i}{2}\hat{\sigma}_i^z + \sum_{i<j}\frac{\pi J_{ij}}{2}\hat{\sigma}_i^z\hat{\sigma}_j^z, \tag{1}$$

where $\omega_i = \gamma_i B_0$, with gyromagnetic ratio $\gamma_i$ of the $i$-th nuclear spin and static magnetic field $B_0$ aligned along $z$-axis, is the Larmor angular frequency, and $J_{ij}$ is the scalar coupling strength between the $i$-th and $j$-th spins.




| | $^{13}$C | $^1$H | $T_1$(s) | $T_2$(s) |
|---|---|---|---|---|
| $^{13}$C | -7787.9 | 215.09 | 18.8 | 0.35 |
| $^1$H | 215.09 | -3206.5 | 10.9 | 3.3 |

**Fig. 1.** $CHCl_3$ as an example of a two-qubit sample with relevant parameters. The $^{13}$C and $^1$H nuclear spins serve as two qubits. The chemical shift (Hz) and $J$-coupling strength are given by the diagonal and off-diagonal terms in the right table, respectively. Two important parameters characterizing the longitudinal and transverse coherence properties represented by $T_1$ and $T_2$ (see more details in the Subsection 2.4) respectively are also provided.

### 2.1. Initialization

To emulate a quantum system of interest, the first step should be the preparation of an initial state of the simulated system. According to the Boltzmann distribution, the system is in the thermal equilibrium state under the room temperature, which is unpolarized (see Fig. 2(a)). However, it is impossible to cool down to extremely low temperature so as to obtain a state polarized into ground state in the liquid-state NMR. Instead, a pseudo-pure state (PPS)[20,21] is widely adopted

$$\hat{\rho}_{\mathrm{PPS}} = \frac{1-\varepsilon}{2^n}\hat{I} + \varepsilon|00\cdots\rangle\langle 00\cdots|, \tag{2}$$

where $\hat{I}$ is the identity matrix and $\varepsilon \sim 10^{-5}$ represents the polarization (see Fig. 2(b)). The validity of using PPS is based on the fact that the identity term is undetectable to the measurement and it is invariant under unitary operations such as free Hamiltonian evolution and pulses control. As a result, the dynamical behavior of PPS is identical to that of a pure state up to a scalar factor. The PPS can be created by several techniques like spatial averaging,[20] logical labelling,[21] temporal averaging,[22] and cat-state.[23] Unfortunately, these methods, which lead the signal to decay exponentially as a function of the number of qubits, fail to scale. This is caused by the non-unitary transformations inevitably involved when creating PPS from thermal equilibrium which shares no common eigenstates with PPS. One scalable approach algorithmic cooling has been investigated in Ref. [24].

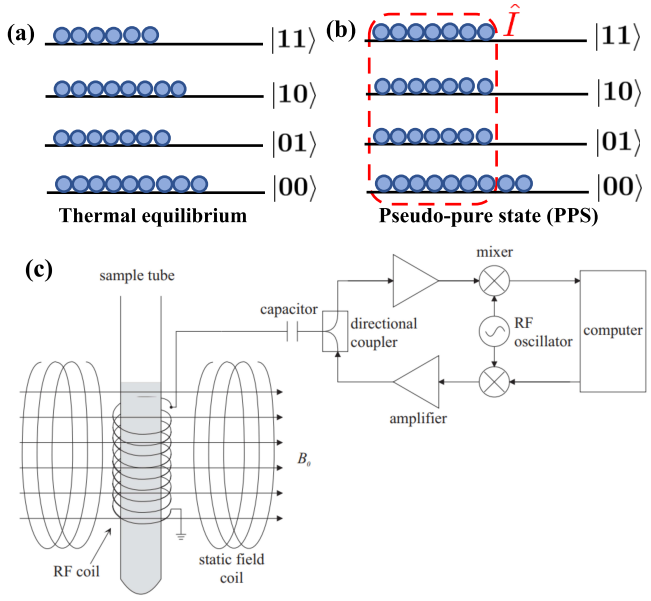



**Fig. 2.** Pseudo-pure state in initialization and the schematic diagram of experimental setup. For a two-qubit system in the thermal equilibrium, there is no available polarized state to employ, as shown in (a). While a PPS, as illustrated in (b), with an identity part and a tiny amount of extra population in the ground state is valid to be treated as an initialized state. (c) Gate control and the measurement are implemented by the RF coil with the following electrical circuit connected to the computer. On the other hand, the external field $B_0$ is generated by the static field coil. This subfigure is adapted from Ref. [26].

### 2.2. Universal gates

Subsequently, the initial state evolves under the desired unitary evolution $\hat{U}(t) = \mathrm{e}^{-\mathrm{i}\hat{H}t}$ which can be decomposed piecewise by utilizing the Trotter formula to the first order[25]

$$\hat{U}(t) = \left(\mathrm{e}^{-\mathrm{i}\sum_n \hat{H}_n \Delta t}\right)^m \approx \left(\prod_n \mathrm{e}^{-\mathrm{i}\hat{H}_n \Delta t}\right)^m, \tag{3}$$

where $t = m\Delta t$ is broken up into $m$ slices with duration $\Delta t$ and the Hamiltonian is assumed to be the sum of local interactions terms $\hat{H} = \sum_n \hat{H}_n$. As $\Delta t \to 0$, the second-order and higher terms are negligible. In other words, the price for the accurate approximation is the large number of quantum gates. Thus, the Hamiltonian engineering is reduced to the implementations of the unitary gates based on local interactions $\mathrm{e}^{-\mathrm{i}\hat{H}_n t}$.

In the case of NMR, the unitary gates of each qubit are carried out by the external radio-frequency (RF) pulses (see Fig. 2(c)), which can be written as

$$\hat{H}_{\mathrm{rf}} = -\gamma B_1 \left[\cos(\omega_{\mathrm{rf}} t + \varphi)\,\hat{\sigma}_i^x - \sin(\omega_{\mathrm{rf}} t + \varphi)\,\hat{\sigma}_i^y\right], \tag{4}$$

where $B_1$, $\omega_{\mathrm{rf}}$, $t$, and $\varphi$ are the amplitude, frequency, length, and phase of the RF pulse, respectively. By tuning these four parameters properly, the rotations about any arbitrary axis with an arbitrary angle can be approximated. More concretely, if the RF is resonant with the Larmor frequency of the spin, i.e., $\omega_{\mathrm{rf}} = \omega_0$, and move to the rotating frame at frequency $\omega_{\mathrm{rf}}$, the first term of NMR Hamiltonian Eq. (1) vanishes and the RF Hamiltonian Eq. (4) becomes time-independent. A unitary evolution is therefore of the form $\hat{U}(t) = \exp[\mathrm{i}\gamma B_1 (\cos\varphi\hat{\sigma}_x - \sin\varphi\hat{\sigma}_y)t]$, which clearly shows how the parameters of the RF pulse determine a quantum gate. For the single-qubit unitary transformation, Bloch's theorem allows the further decomposition into rotations about two fixed axes $\hat{U}(t) = \mathrm{e}^{\mathrm{i}\alpha}\hat{R}_x(\beta)\hat{R}_y(\gamma)\hat{R}_x(\delta)$, where $\alpha, \beta, \gamma, \delta$ are real numbers and $\hat{R}_x(\beta)$ specifies the rotation around $x$-axis for angle $\beta$. The ability to implement single-qubit rotations and controlled-NOT (CNOT) gate enables the universal quantum gates.[26] However, in reality, the relaxation renders conventional composite pulses inaccurate in large-size systems, especially in the relatively long durations. Capitalizing on the recent advances in optimized pulse engineering techniques inspired by optimal control theory for NMR quantum computing, one is able to attain ultra-high precision not only in the systems of limited scale. The representative one is the gradient ascent pulse engineering (GRAPE) technique.[27]

### 2.3. Measurement

Finally, with the aid of an RF coil, the transverse magnetization of the ensemble can be obtained. This detection coil is weakly coupled to the nuclear spins so that it barely contributes to the decoherence. However, there remain interactions with the heat bath and inhomogeneity of the static field, which still leads to the decoherence of the nuclear spins. Consequently, the measurement of the nuclear spins is based on the free induction decay (FID). What FID experiments yield are the expectation values of readout operators in the $x$–$y$ plane, and finally, the time-domain FID signals are converted to frequency-domain NMR spectra via Fourier transform. Though such weak measurement is unable to provide as much information of a single spin as the projective measurement, the ensemble-averaged information can be distilled. For the complete description of the state, i.e., all elements of the density matrix, one should resort to the full quantum state tomography.[13,28]

### 2.4. Decoherence

The decoherence originates from the unwanted interactions with the environment, which leads to the loss of information carried by qubits. As a result, the coherence is a crucial facet of examining whether a quantum system would be entitled to be the physical implementation of a quantum simulator. For the decoherence stemming from the couplings between the spins and the lattice, it is conventionally characterized by the energy relaxation (or longitudinal relaxation) time $T_1$, which is about tens of seconds in a liquid sample. Whereas phase randomization time (or transverse relaxation) $T_2$ characterizes the decoherence resulting from the spin–spin couplings. In NMR systems, a more important parameter is denoted by $T_2^*$, which is extracted from FID experiments and in turn is termed inhomogeneous dephasing time. The $T_2^*$ is supposed to be long enough during which the sequences of gates can be implemented. For the complex tasks, the more advanced techniques should be applied to extend $T_2^*$ so that preserve the information, such as RF selection which improves the $T_2^*$ at the cost of signal loss.[29,30]

## 3. Many-body physics

### 3.1. Quantum chaos

In the classical systems, the integrable and non-integrable systems are related to the regular and chaotic motions, respectively, where the latter display the butterfly effect that the initial diminutive deviations may give rise to considerable differences in a later time. Correspondingly, in the quantum scenario, a small perturbation that spreads over a many-body system may result in large commutators with the operators which are commutative with the perturbation initially.[31] Formally, the quantum version of butterfly effect is relevant to a core concept termed quantum information scrambling, that is, the information stored in local degrees of freedom smears over global degrees of freedom. Scrambling lies at the heart of the dynamics of quantum information.[32] From the experimental perspective, it can be understood by a key observable

named out-of-time correlator (OTOC), which first appeared in the context of superconductivity[33] and was defined as

$$F(t) = \langle \hat{W}^{\dagger}(t)\hat{V}^{\dagger}(0)\hat{W}(t)\hat{V}(0)\rangle, \tag{5}$$

where $\hat{W}(t) = e^{i\hat{H}t}\hat{W}(0)e^{-i\hat{H}t}$ is the operator $\hat{W}$ in the Heisenberg picture, and $\hat{W}(0)$ and $\hat{V}(0)$ are two commutative local Hermitian operators.

From the connection $\mathrm{Re}[F(t)] = 1 - \langle|[\hat{W}(t), \hat{V}(0)]|^2\rangle/2$, it is easier to understand how OTOC illuminates the insights into quantum chaos. $F(t)$ represents the non-commutativity degree between two local operators $\hat{W}(t)$ and $\hat{V}(t)$, whose commutator is zero initially, under the time evolution according to the interaction introduced by the Hamiltonian $\hat{H}$. To better appreciate it, one may have a closer look at $\hat{W}(t)$, which can be expanded as a sum of nested commutators

$$\begin{aligned}\hat{W}(t) = \hat{W} + it[\hat{H}, \hat{W}] - \frac{t^2}{2!}[\hat{H}, [\hat{H}, \hat{W}]] \\ - \frac{it^3}{3!}[\hat{H}, [\hat{H}, [\hat{H}, \hat{W}]]] + \cdots .\end{aligned} \tag{6}$$

As time grows, while the high-order terms are getting significant, the expression of $\hat{W}(t)$ becomes more and more complicated and might finally fail to commute with an initially commutative operator $\hat{V}$. Hence, the growth of simple localized operators may lead to non-commutativity with almost all other operators in the system on the long time scale, which bears striking resemblance to the butterfly effect.

From the perspective of quantum information, it is a crucial task to protect the information from delocalization in the quantum channels,[34] which bears directly on the fault-tolerance and computation capability of quantum channels. Since a quantum channel is defined as a completely-positive and trace-preserving linear map from one to another Hilbert space, a unitary transformation for the initial density matrix $\hat{\rho}_0$ of the form $\hat{W}(t)\hat{\rho}_0\hat{W}^{\dagger}(t)$, with $\hat{W}(t)$ being the Heisenberg operator of a local Hermitian operator, is exactly an example of quantum channel. Consequently, the OTOC can be construed as the expectation value of local measurement of observable $\hat{V}$ on the final state of the density matrix which goes through the quantum channel determined by local operator $\hat{W}(t)$, i.e.,

$$\langle F(t)\rangle \propto \mathrm{Tr}\left[\hat{W}(t)\hat{\rho}_0\hat{W}^{\dagger}(t)\hat{V}\right]. \tag{7}$$

Experimentally, the final readout is accessible, whereas the evolution of local operator $\hat{W}$ involves the time reversal of the many-body Hamiltonian, which is challenging. Fortunately, borrowing the protocol that is well familiar with the NMR experimental physicists in the form of Hahn spin echoes,[35] together with the Trotter formula given by Eq. (3), the backward time-evolution can also be realized. The first two parallel experiments to measure OTOC were done with the NMR[36] and trapped-ion[37] respectively.

### 3.1.1. Integrable and non-integrable systems

The distinct behaviors of integrable and non-integrable systems can be observed via OTOC.[36] Take the paradigmatic one-dimensional transverse-field Ising chain (TFIC) model as an example, whose Hamiltonian reads as

$$\hat{H} = \sum_i \left(-J\hat{\sigma}_i^z\hat{\sigma}_{i+1}^z + g\hat{\sigma}_i^x\right), \tag{8}$$

where $J$ represents the coupling strengths of nearest-neighbor interaction, and $g$ is the uniform transverse field. This is an integrable Hamiltonian. If $h\hat{\sigma}_i^z$ is added into Eq. (8) with $h \neq 0$ while $g \neq 0$, the Hamiltonian is otherwise non-integrable. As illustrated in Fig. 3(a), there is an oscillation of OTOC for the integrable system. By contrast, in the case of non-integrable system shown in Fig. 3(b), all OTOCs feature a decay to some values around zero after a long time, which suggests that the information is no longer retrievable to the local measurement.

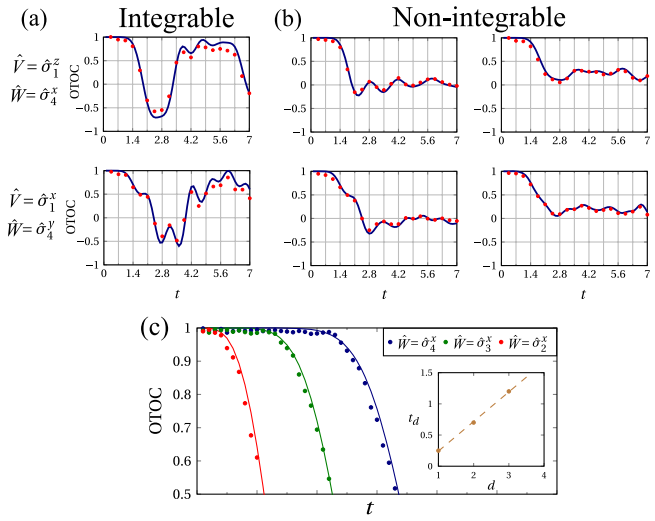



**Fig. 3.** Distinct behaviors of (a) integrable ($g = 1$, $h = 0$) and (b) non-integrable ($g = 1.05$, $h = 0.5$ for left column and $g = 1$, $h = 1$ for right column) cases of Ising spin chain model are distinguished by OTOC $F(t)$. (c) Measurement of butterfly velocity. The OTOCs for three different operators $\hat{W}_j$ are shown with different colors. The inset shows the characteristic time $t_d$ versus the distance $d$ between two operators, where the butterfly velocity $v_B$ can be obtained according to $t_d = d/v_B + c$ with $c$ being the intercept. The figures are adapted from Ref. [36].

### 3.1.2. Butterfly velocity

Another intuitive result comes from the early-time behaviors of OTOCs. If one chooses different local operators $\hat{W}_j(t)$ as the time-dependent ones while fixing the initial operator $\hat{V}(0)$, these OTOCs of different operators serve as a tool to estimate the speeds of correlations spreading over the system. Intuitively, the further $\hat{W}_j$ is away from where $\hat{V}$ resides, the longer the time that the correlation takes to arrive at $\hat{W}_j$'s site. Actually, this is what is observed in the experiments with a 4-qubit NMR simulator.[36] In the case of Ising spin chain model, let $\hat{V} = \hat{\sigma}_i^{\alpha}$ and $\hat{W}_j = \hat{\sigma}_{i+j}^{\beta}$, where $\alpha, \beta = x, y, z$ and $i, j = 1, 2, 3, \ldots$ are the labels of spin sites. Larger $j$ does lead to later decay of OTOC, which coincides with the longer correlation arrival time, see Fig. 3(c). Nevertheless,

although the arrival time is dependent on the specific operator, the propagating velocity of correlations is expected to be operator-independent in a certain system. This velocity is characterized by $v_B$, which is called butterfly velocity.[34,38] And the characteristic time $t_d = d/v_B$, defined in terms of the distance between two operators $d$ and the butterfly velocity $v_B$, signals the onset of chaos where the OTOC is different from unity. Based on this relation, the butterfly velocity can be extracted as shown in the inset of Fig. 3(c). In the systems where only short-range interactions exist, analogous to the finite velocity of linear information spreading in relativistic theories, the butterfly velocity defines an effective light cone, within which the correlations are limited to. And the butterfly velocity is related to a more general bound known as Lieb–Robinson bound.[39,40]

In the classical chaotic system, the separation of two initially close trajectories in the phase-space increases exponentially in the time evolution $|\Delta \boldsymbol{x}(t)| \approx |\Delta \boldsymbol{x}(0)| e^{\lambda_L t}$. Therefore, the positive Lyapunov exponent $\lambda_L$ indicates the divergence of the system. Similarly, in the early-time evolution of non-integrable systems, the OTOCs can be formulated by $F(t) = a - b e^{\lambda_Q (t - t_d)} + \cdots$, where $a, b$ are non-universal constants, $\lambda_Q$ is the quantum analogy with Lyapunov exponent[41] which likewise serves as a proxy for quantum chaos. What is more, the quantum Lyapunov exponent is bound by $\lambda_L \leq 2\pi/\beta$, as the information scrambling rate bound in black holes,[42,43] where $\beta^{-1} = 2k_B T$ is the inverse temperature. This remarkable coincidence brings about the intriguing conjecture that any quantum system that saturates the Lyapunov exponent bound is holographic dual to a black hole.[44]

### 3.2. Quantum phase transition

#### 3.2.1. Many-body localization and Anderson localization phases

Another aspect in connection with the scrambling of information is the thermalization and entanglement entropy. To be more concrete, consider an initial state which is the direct product of two pure subsystems, say A and B, and undergoes an evolution governed by a chaotic Hamiltonian. After a time longer than the thermalization time, the output state turns out to be highly entangled, which suggests that each subsystem is near maximally mixed and thus, corresponds to a thermal ensemble regarding all local measurement observables.[45] Moreover, the degree of entanglement between subsystems can be quantified by the growth of local von Neumann entropy

$$S_{EE} = -\mathrm{Tr}\left(\hat{\rho}_A \log_2 \hat{\rho}_A\right), \tag{9}$$

where $\hat{\rho}_A$ is the reduced density matrix by tracing out subsystem B. As the classical entropy is an extensive quantity, entanglement entropy also increases proportionally to the size of the subsystem. In this sense, the entanglement entropy plays a role akin to the thermal entropy in classical statistical mechanics which indicates the chaotic degree of the system.[46] As a result, entanglement entropy can be a metric to differentiate the phases with different strengths of entanglement such as many-body localization (MBL) and Anderson localization (AL).

MBL is a regime where the entanglement entropy scales logarithmically.[47] This localization results from the strong disorder that struggles against the thermalization and accordingly suppresses the growth of entanglement entropy. Whereas the non-interacting correspondence AL has a saturation as the primary signature (see the dashed lines with non-zero (zero) interaction strength, the right axis in Fig. 4).

Nevertheless, measuring entanglement entropy is challenging, the pioneering work was achieved only on the small number of particles.[48] Recently, the average correlation length $L_c$ as an alternative has been demonstrated on the NMR platform as effective as entanglement entropy[49] (see experimental results (dotted lines) and simulation (solid lines), left axis in Fig. 4). The $L_c$ is referred to the contributions of all possible spin correlations with Hamming weight.[50] Armed with the coherent averaging techniques[51] to tune both the interaction strength and the degree of disorder, the average correlation length can be extracted from the intensity of multiple quantum coherence (MQC) based on the measurement of OTOCs.

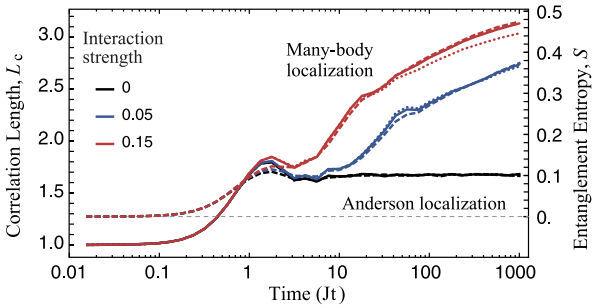



**Fig. 4.** Simulations of entanglement entropy and correlation length for many-body localization and Anderson localization. As the increment of interaction strength, the MBL emerges, featured by a slow growth in time of $L_c$ (solid lines, left axis), which is consistent with the approximated $L_c$ obtained by measuring OTOC (dotted lines, left axis), the logarithmic growth of entanglement entropy (dashed lines, right axis). By pronounced contrast, in the AL phase where the interaction is absent (the black lines corresponding to zero interaction strength), $L_c$ is saturated. The figure is adapted from Ref. [49].

#### 3.2.2. Paramagnetic and ferromagnetic phases

As an indicator, OTOC also outperforms some other kind of correlators with respect to detecting equilibrium quantum phase transition (EQPT) and dynamical quantum phase transition (DQPT),[52] because OTOC captures the scrambling of quantum information, and both EQPT and DQPT attend rapid spread of quantum information on account of appreciable quantum fluctuations.

The 1D transverse-field Ising chain (TFIC) model in Eq. (8) is considered with periodic boundary condition. Autocorrelation function $\chi(t) = \langle \hat{\sigma}_i^z(t)\hat{\sigma}_i^z \rangle$ allows one to detect the ordered phase in equilibrium from dynamics, as it vanishes in the paramagnetic phase ($g > J$) while taking a nonzero value in the ferromagnetic phase ($g < J$), in the long-time limit. Unfortunately, the autocorrelation function fails to serve its turn in the case of a quantum quench.[53] To gain a full picture of quantum information dynamics, the natural alternatives are the higher-order correlations, say the second moment, i.e., $\langle (\hat{\sigma}_i^z(t)\hat{\sigma}_i^z)^2 \rangle$, which is exactly a special case of OTOC in Eq. (5), where $\hat{V} = \hat{W} = \hat{\sigma}_i^z$.[54]

Another candidate is the two-body correlation function $C(t) = \left\langle \hat{\sigma}_i^z(t)\hat{\sigma}_j^z(t) \right\rangle (i \neq j)$. Though the two-body correlation function has been exploited to study DQPTs in the non-integrable ferromagnetic axial next-nearest-neighbor Ising (ANNNI) model, the accuracy and robustness remain unsatisfactory.[55] As an extension of the integrable TFIC model, the ANNNI model has also been extensively investigated, where the next-nearest-neighbor interactions $\Delta \hat{\sigma}_i^z \hat{\sigma}_{i+2}^z$ are involved in Hamiltonian Eq. (8) and $\Delta$ denotes the next-nearest-neighbor couplings.

In a recent work,[56] the advantages of OTOC have been demonstrated compared with autocorrelation and two-body correlation function with respect to detecting DQPT and locating the critical point in EQPT.

The routine of examining DQPT by a quantum quench is as follows: first, the system is initialized into its ground state of the initial Hamiltonian. Next, a sudden change, say a Hamiltonian $\hat{H}_{\rm q}$ whose eigenstates are different from the ground state, is imposed. Subsequently, the system evolves under $\hat{H}_{\rm q}$ accordingly. Finally, some order parameters are measured.[57] Particularly, in the Ising model, the Hamiltonian with $g = 0$ in Eq. (8) was chosen as the initial Hamiltonian. It then follows that the initial state is one of the fully polarized ground states. Since the behavior of order parameters in one dynamical phase is supposed to be distinct from that in other phases, the quenches of Hamiltonians with $g < g_{\rm c}$ and $g > g_{\rm c}$, where $g_{\rm c}$ denotes the critical value of the uniform transverse field, were performed respectively. As the system quenches across $g_{\rm c}$, there is a phase transition. Therefore, DQPT only occurs when the system governed by the quenched Hamiltonian in the different phase from the ground state phase.

Well in accord with the theoretical simulation, the dynamics of OTOC exhibits sharp distinctions between ferromagnetic ($g < g_{\rm c}$) and paramagnetic dynamical phases ($g > g_{\rm c}$). As illustrated in the top panel of Fig. 5(a), OTOC stays at certain positive value with comparatively small fluctuations in the $g < g_{\rm c}$ region, whereas it oscillates around zero in the other. It is hence experimentally confirmed that the OTOC fulfills the job that distinguishes different dynamical phases and, in turn, diagnoses DQPT. On the other hand, the autocorrelation function (see the middle panel in Fig. 5(a)), without notable contrast between the two phases, is unable to reveal DQPT unambiguously. Furthermore, these results still hold for the non-integrable ANNNI model as shown in Fig. 5(b).

Although the two-body correlation function (see the bottom panel in Fig. 5(a)) behaves similarly as OTOC, if one delves into the critical point in EQPT, which can be identified by the time-averaging OTOC $\bar{F} = (1/t)\int_{\tau=0}^{t} F(\tau)\mathrm{d}\tau$ in the Ising model, the two-body correlation is also defeated by OTOC. In both theoretical and experimental results given in Fig. 5(c) (Fig. 5(d)) for integrable (non-integrable) system respectively, OTOC displays a more noticeable turning point at the critical point. Besides, it also has been shown that the OTOC is more robust to the decoherence than the two-body correlation.[56]

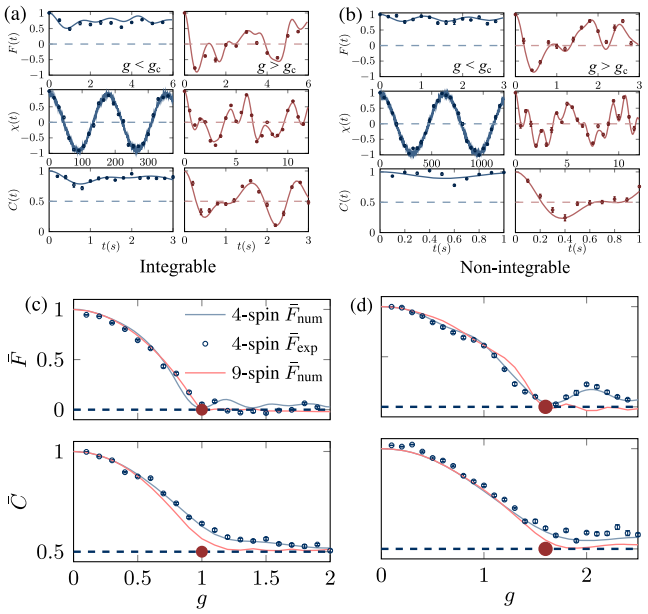



**Fig. 5.** Experimental results of DQPT and EQPT for integrable and non-integrable systems. The comparisons of the OTOC $F(t)$ (top panels), autocorrelation $\chi(t)$ (bottom panels), and two-body correlation function $C(t)$ (bottom panels) to detect DQPT in the integrable system and non-integrable system represented by (a) TFIC model and (b) ANNNI model, respectively. Critical points of (c) TFIC model and (d) ANNNI model are marked as the turning points of the long-time averaged OTOC $\bar{F}$ (top panels) and two-body correlation $\bar{C}$ (bottom panels) as functions of the transverse field strength $g$. The figures are adapted from Ref. [56].

## 4. Quantum gravity

### 4.1. Ads/CFT correspondence

#### 4.1.1. Ryu–Takayanagi entropy

As discussed above, the OTOC has underlying connections with Ads/CFT duality. On this account, Ads/CFT correspondence links the quantum gravity theory and quantum information theory[58] meanwhile inspiring the incorporation of holographic entanglement entropy into the study of quantum

gravity. Specifically, the entanglement entropy of the boundary system can be related to the bulk geometry in terms of Ryu–Takayanagi formula,[59,60] which reads as

$$S_{\mathrm{EE}}(\mathcal{A}) = \frac{Ar_{\min}}{4G_{\mathrm{N}}}, \tag{10}$$

where $\mathcal{A}$ denotes a $(d-1)$-dimensional region and $Ar_{\min}$ is the area of the bulk $(d-2)$-dimensional minimal surface anchored to $\mathcal{A}$, and $G_{\mathrm{N}}$ is the Newton constant.

### 4.1.2. Tensor network

On the other hand, the tensor network (see Fig. 6) serving as an ideal ground to realize AdS/CFT enables the exploration of AdS/CFT on quantum simulators. And the building blocks of tensor network are the perfect tensors, as illustrated in Fig. 7(a). For instance, a rank-6 perfect tensor is a 6-qubit state on a hexagon such that any three-qubit subsystem is maximally entangled with the rest. Let $|\psi(n)\rangle$ denote the perfect tensor at a hexagon node $n$, then the total tensor network state $|\Psi\rangle$ takes the form

$$|\Psi\rangle = \otimes_{\ell}\langle\ell| \otimes_{n} |\psi(n)\rangle, \tag{11}$$

where each link $|\ell\rangle = (|00\rangle + |11\rangle)/\sqrt{2}$ is the maximally-entangled state and the inner products are taken at the end points of each link $\ell$. A realization on a 6-qubit NMR quantum simulator showed[61] that one only needs to call Hadamard gates and controlled-$Z$ gates into play, a rank-6 perfect tensor can be constructed from the initialized state $|0\rangle^{\otimes n}$ with satisfactory fidelity.

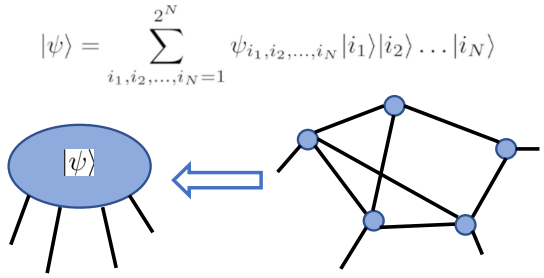



**Fig. 6.** Diagrammatic representation of a tensor network. The coefficients of an $N$-body system amount to an $N$-order tensor. A tensor network represents the structure and the amount of entanglement of a quantum many-body state. The tensors are linked by the lines, which correspond to the indices $i_1, i_2, \ldots, i_N$. Then, the contracted (summed) common indices are represented by the lines connecting to shapes. Then, a tensor network with $m$ unpaired legs can be treated as an $m$-order tensor. In this sense, the tensor network representation reduces the complexity of quantum many-body problem.

If a tensor network is made of perfect tensors, its entanglement entropy is as Eq. (9), and $S_{\mathrm{EE}}^{(k)}$ equals the minimal number of cuts by virtual surfaces $\mathcal{S}$, which is the discrete counterpart of Eq. (10).[62] For example, the $\mathcal{S}$ is chosen to be the one shown in Fig. 7(b) and the minimal number of cuts is three, it yields a rank-6 perfect tensor where the number of boundary qubits is also three, the same as that of bulk qubits. Experimentally, $S_{\mathrm{EE}}^{(k)}$ is nothing but Von Neumann entropy, hence it holds that $S_{\mathrm{EE}}^{(k)} = -\mathrm{Tr}\left(\hat{\rho}_m^{(k)} \log_2 \hat{\rho}_m^{(k)}\right) = k$, where $\hat{\rho}_m^{(k)}$ is the reduced density matrix by tracing out $m$ qubits and $k+m=6$.

Moreover, when $k \leq 3$, the reduced density matrix equals an identity and on the other side $S^{(k)} = \min\{k, 6-k\}$, which has also been verified,[61] with the proper refinements by taking account of the decoherence, as shown in Fig. 7(c). It is noteworthy that the compensations of decoherence errors were accomplished by performing 6-qubit full tomography, which is the largest full state characterization in an NMR system to date.

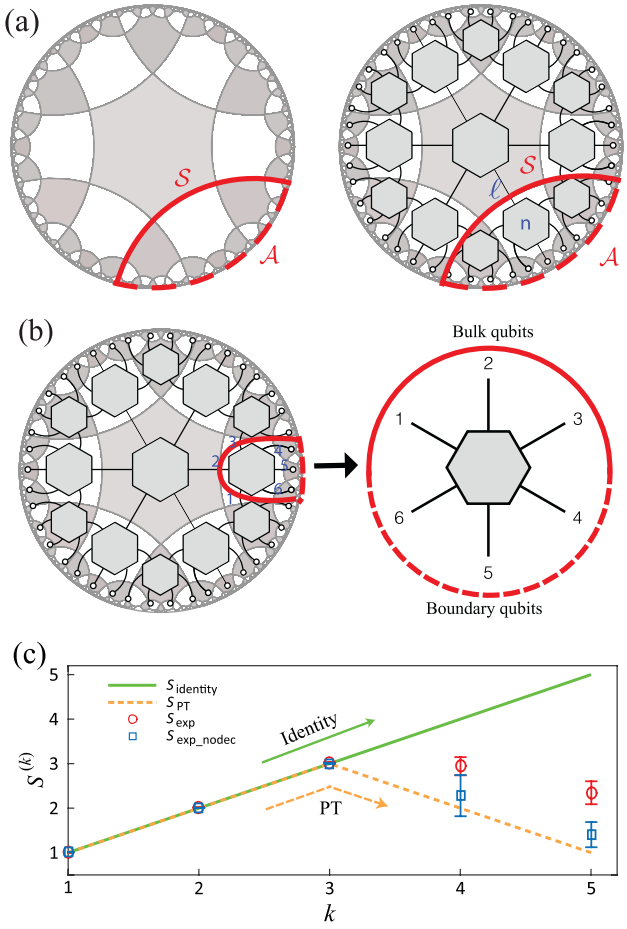



**Fig. 7.** Illustration of tensor network and perfect tensor, and the theoretical and experimental results of RT entropy. (a) The disk is a two-dimensional ads with the hexagonal tiling. The solid arc marks the minimal surface $\mathcal{S}$ which is anchored to the two ends of the boundary region $\mathcal{A}$ illustrated by the dashed line. The tensor network on the right side is the discrete version of the left ads space. The tensor network is composed of rank-6 tensors represented by a hexagonal node with the links $\ell$, each of which corresponds to a maximally-entangled state. The total tensor network state is obtained by taking inner products in $\mathcal{H}$, corresponding to connecting legs of nodes to links. (b) A rank-6 perfect tensor with three minimal cuts by virtual surface illustrated by the red solid line. Half of six qubits are bulk qubits and the other half are at boundary. (c) The theoretical results of entanglement entropy $S^{(k)}$ equalling to $\min\{k, 6-k\}$ are shown by orange dashed line. The refined experimental results with the compensation of decoherence represented by blue squares are consistent with the theory much better than initial results shown by red circles. The maximal entropy of a $k$-qubit subsystem by assuming a 6-qubit identity is plotted in green dotted line as an upper-bound reference. The figures are adapted from Ref. [61].

### 4.2. Loop quantum gravity

In another aspect of quantum gravity, the nuclei spin states in NMR can also be employed to simulate quantum geometries of spacetime.

#### 4.2.1. Spin network

In loop quantum gravity, the quantum states endowed with discrete geometries of quantum spacetime at the Planck scale are represented by spin networks.[63] The time evolution of spin network[64] builds up a $(3+1)$-dimensional quantum spacetime, then the boundary of which is the spin network.

A spin network state is characterized by an oriented graph $\Gamma$ with half-integer $j_l$ labelling a $(2j_l+1)$-dimensional $SU(2)$ irreducible representation and the invariant tensor $|i_n\rangle$ on each node $n$ which is invariant under $SU(2)$ action. The spin network state is formally defined as $|\Gamma, j_l, i_n\rangle := \otimes_n |i_n\rangle$, where $\otimes_n$ denotes the tensor product of invariant tensors at all nodes. Since the simulation of a tensor $|i_n\rangle$ is experimentally tractable, and such a spin network with $m$ nodes is equivalent to creating $m$ invariant tensors in the experiment, it enables the simulation of spin network.

In particular, what a 4-qubit invariant-tensor state represents is a quantum tetrahedron $N=4$ corresponding to the node of the spin network.[65] The high-fidelity (over 95%) preparation of ten quantum tetrahedrons has been achieved by an NMR simulator, identified by quantum tetrahedrons' geometric properties through measuring dihedral angles.[66] The geometry properties of quantum tetrahedron are encoded in the quantum angular momenta $\hat{\boldsymbol{J}}^{(k)} = (\hat{J}_x^{(k)}, \hat{J}_y^{(k)}, \hat{J}_z^{(k)})$, thus, in terms of which the dihedral angle allows one to reconstruct quantum tetrahedron. More precisely, the dihedral angle $\phi_{km}$ and the angle of normals $\theta_{km}$ between the $k$-th an $m$-th faces have the relation $\cos\phi_{km} = -\cos\theta_{km}$, where the latter is quantized as $\widehat{\cos\theta}_{km} = \frac{4}{3}\hat{\boldsymbol{J}}^{(k)} \cdot \hat{\boldsymbol{J}}^{(m)}$,[67] while on the other hand it can be written in favor of Pauli matrices $\widehat{\cos\theta}_{km} = \left(\hat{\sigma}_x^k \hat{\sigma}_x^m + \hat{\sigma}_y^k \hat{\sigma}_y^m + \hat{\sigma}_z^k \hat{\sigma}_z^m\right)/6$. Examining the dihedral angles which bridge theoretical geometries and experimental observables, the shape of prepared quantum tetrahedrons was verified.

#### 4.2.2. Dynamics of quantum geometry

In addition, the local dynamics of quantum geometry is studied by vertex amplitude, which is defined as $A(i_1,\ldots,i_5) = \otimes_{\ell=1}^{10} \langle \ell | \otimes_{n=1}^{5} | i_n \rangle$. This is much similar as Eq. (11), where the perfect tensor is replaced by invariant tensor state with $|\ell\rangle = (|01\rangle - |10\rangle)/\sqrt{2}$ and the left-hand side of the equation becomes the vertex amplitude.

Vertex amplitudes determine the spinfoam amplitudes, which are the transition amplitudes between the initial and the final spin networks.[68] In principle, if the two-qubit maximally entanglement states can be established between arbitrary two tetrahedra, as illustrated in Fig. 8, the vertex amplitudes can be obtained by evaluating the inner product between five quantum tetrahedra states. However, it is beyond the present manageable level for a 20-qubit quantum computer. Instead, the full tomography is also helpful, through which the information about quantum tetrahedra is acquired.[66]

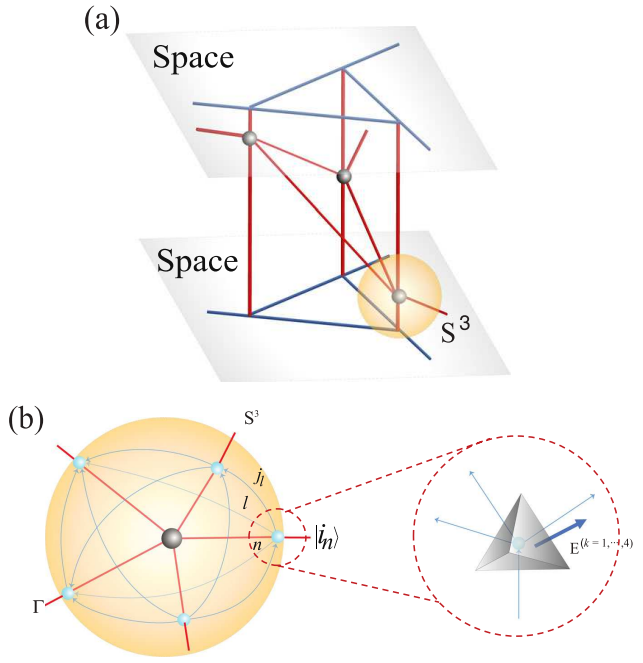



**Fig. 8.** Spin network and quantum tetrahedra. (a) In a $(3+1)$-dimensional dynamical quantum spacetime, a 3-sphere $S^3$ encloses a portion of quantum spacetime surrounding a vertex (in black) where the world sheets meet. (b) A spin network (blue) is represented by the intersection between world sheets and $S^3$. Each node of spin network corresponds to a quantum tetrahedron associated with an invariant tensor state $|i_n\rangle$. Five tetrahedra are glued through the faces dual to the links to form a closed $S^3$, represented by the connections of links $l$, each of which carries a half-integer $j_l$. The figures are adapted from Ref. [66].

## 5. Outlook

Apart from the achievements discussed above, NMR simulations also provide new insights into various subjects (see Fig. 9) such as quantum state tomography,[69–73] quantum algorithm,[74–76] non-Abelian topological orders,[77,78] Sachdev–Ye–Kitaev model,[79] prethermalization,[80] disordered systems,[81] probabilistic quantum cloning,[82] eigenproblem solving,[83] anti-PT-symmetry,[84] and even photosynthetic light harvesting.[85] However, on the theoretical side, the theories of decoherence and control are required; on the experimental side, the controllability and scalability of the system remain scope to improve. In particular, the spectral crowding that occurs as the number of energy levels increases exponentially with the increasing number of spins hinders liquid NMR from scalability. Though in solid-state NMR, the scalability drawback may be overcome to some extent, the manipulation and measurement of single qubit would be difficult. A promising alternative is the nitrogen-vacancy (NV) centers in

diamond, into which the well-developed techniques in controlling spins in NMR have been incorporated.[86]

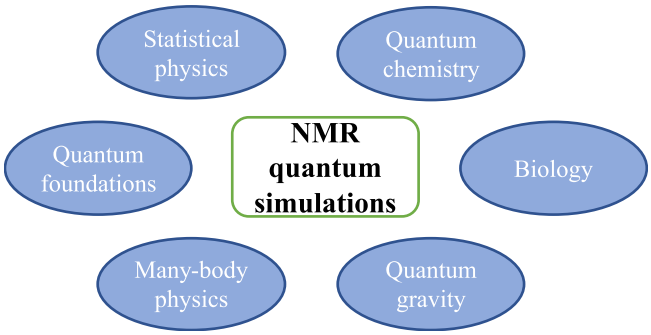



**Fig. 9.** Fields on which the NMR simulations shed light.

The progress on quantum simulation tempts us to envisage that the practical simulators will be built in the near future as the prototype of full-fledged quantum computers. Especially when the point beyond which the classical computer would be inferior to quantum simulations is marked, at least in some cases, it would be a milestone for both physics and computer science.

## References


[1] Houck A A, Türeci H E and Koch J 2012 *Nat. Phys.* **8** 292
[2] Wendin G 2017 *Rep. Prog. Phys.* **80** 106001
[3] Barreiro J T, Müller M, Schindler P, Nigg D, Monz T, Chwalla M, Hennrich M, Roos C F, Zoller P and Blatt R 2011 *Nature* **470** 486
[4] Blatt R and Roos C F 2012 *Nat. Phys.* **8** 277
[5] Lewenstein M, Sanpera A, Ahufinger V, Damski B, Sen A and Sen U 2007 *Adv. Phys.* **56** 243
[6] Bloch I, Dalibard J and Nascimbene S 2012 *Nat. Phys.* **8** 267
[7] Saffman M 2016 *J. Phys. B: Atom. Mol. Opt. Phys.* **49** 202001
[8] Angelakis D G 2017 *Quantum Science and Technology* (Springer)
[9] Flamini F, Spagnolo N and Sciarrino F 2018 *Rep. Prog. Phys.* **82** 016001
[10] Buluta I, Ashhab S and Nori F 2011 *Rep. Prog. Phys.* **74** 104401
[11] Childress L and Hanson R 2013 *MRS Bulletin* **38** 134
[12] Georgescu I M, Ashhab S and Nori F 2014 *Rev. Mod. Phys.* **86** 153
[13] Chuang I L, Vandersypen L M, Zhou X, Leung D W and Lloyd S 1998 *Nature* **393** 143
[14] Jones J A, Mosca M and Hansen R H 1998 *Nature* **393** 344
[15] Somaroo S, Tseng C, Havel T, Laflamme R and Cory D G 1999 *Phys. Rev. Lett.* **82** 5381
[16] Peng X, Zhang J, Du J and Suter D 2009 *Phys. Rev. Lett.* **103** 140501
[17] Zhang J F, Yung M H, Laflamme R, Aspuru-Guzik A and Baugh J 2012 *Nat. Commun.* **3** 1
[18] Lu D W, Li K, Li J, Katiyar H, Park A J, Feng G, Xin T, Li H, Long G L, Brodutch A, Baugh J, Zeng B and Laflamme R 2017 *Npj Quantum Inf.* **3** 48
[19] Li J, Luo Z, Xin T, Wang H, Kribs D, Lu D, Zeng B and Laflamme R 2019 *Phys. Rev. Lett.* **123** 030502
[20] Cory D G, Fahmy A F and Havel T F 1997 *Proc. Natl. Acad. Sci. USA* **94** 1634
[21] Gershenfeld N A and Chuang I L 1997 *Science* **275** 350
[22] Knill E, Chuang I and Laflamme R 1998 *Phys. Rev. A* **57** 3348
[23] Knill E, Laflamme R, Martinez R and Tseng C H 2000 *Nature* **404** 368
[24] Ben-Or M, Gottesman D and Hassidim A 2013 arXiv:1301.1995 [quant-ph]
[25] Trotter H F 1959 *Proc. Am. Math. Soc.* **10** 545
[26] Nielsen M A and Chuang I 2002 *Quantum computation and quantum information* (American Association of Physics Teachers)
[27] Khaneja N, Reiss T, Kehlet C, Schulte-Herbrüggen T and Glaser S J 2005 *J. Magn. Reson.* **172** 296
[28] Chuang I L, Gershenfeld N and Kubinec M 1998 *Phys. Rev. Lett.* **80** 3408
[29] Shaka A, Keeler J, Smith M and Freeman R 1985 *J. Magn. Reson.* **61** 175
[30] Ryan C, Laforest M and Laflamme R 2009 *New J. Phys.* **11** 013034
[31] Hayden P and Preskill J 2007 *J. High Energy Phys.* **2007** 120
[32] Swingle B 2018 *Nat. Phys.* **14** 988
[33] Larkin A and Ovchinnikov Y N 1969 *Sov. Phys. JETP* **28** 1200
[34] Hosur P, Qi X L, Roberts D A and Yoshida B 2016 *J. High Energy Phys.* **2016** 4
[35] Hahn E L 1950 *Phys. Rev.* **80** 580
[36] Li J, Fan R, Wang H, Ye B, Zeng B, Zhai H, Peng X and Du J 2017 *Phys. Rev. X* **7** 031011
[37] Gärttner M, Bohnet J G, Safavi-Naini A, Wall M L, Bollinger J J and Rey A M 2017 *Nat. Phys.* **13** 781
[38] Shenker S H and Stanford D 2015 *J. High Energy Phys.* **2015** 132
[39] Lieb E H and Robinson D W 1972 *Statistical mechanics* pp. 425–431 (Springer)
[40] Roberts D A and Swingle B 2016 *Phys. Rev. Lett.* **117** 091602
[41] Kitaev A 2014 *Talk given at the Fundamental Physics Prize Symposium* Vol. **10**
[42] Shenker S H and Stanford D 2014 *J. High Energy Phys.* **2014** 67
[43] Maldacena J, Shenker S H and Stanford D 2016 *J. High Energy Phys.* **2016** 106
[44] Maldacena J and Stanford D 2016 *Phys. Rev. D* **94** 106002
[45] Lewis-Swan R, Safavi-Naini A, Kaufman A and Rey A 2019 *Nat. Rev. Phys.* **1** 627
[46] Khemani V, Lim S P, Sheng D and Huse D A 2017 *Phys. Rev. X* **7** 021013
[47] Lukin A, Rispoli M, Schittko R, Tai M E, Kaufman A M, Choi S, Khemani V, Léonard J and Greiner M 2019 *Science* **364** 256
[48] Islam R, Ma R, Preiss P M, Tai M E, Lukin A, Rispoli M and Greiner M 2015 *Nature* **528** 77
[49] Wei K X, Ramanathan C and Cappellaro P 2018 *Phys. Rev. Lett.* **120** 070501
[50] Bardarson J H, Pollmann F and Moore J E 2012 *Phys. Rev. Lett.* **109** 017202
[51] Haeberlen U 2012 *High Resolution NMR in solids selective averaging: supplement 1 advances in magnetic resonance* Vol. **1** (Elsevier)
[52] Heyl M, Pollmann F and Dóra B 2018 *Phys. Rev. Lett.* **121** 016801
[53] Essler F H L, Evangelisti S and Fagotti M 2012 *Phys. Rev. Lett.* **109** 247206
[54] Sachdev S 2007 *Quantum Phase Transitions* p. 1
[55] Zhang J, Pagano G, Hess P W, Kyprianidis A, Becker P, Kaplan H, Gorshkov A V, Gong Z X and Monroe C 2017 *Nature* **551** 601
[56] Nie X, Wei B B, Chen X, Zhang Z, Zhao X, Qiu C, Tian Y, Ji Y, Xin T, Lu D and Li J 2020 *Phys. Rev. Lett.* **124** 250601
[57] Žunkovič B, Heyl M, Knap M and Silva A 2018 *Phys. Rev. Lett.* **120** 130601
[58] Maldacena J and Susskind L 2013 *Fortschr. Phys.* **61** 781
[59] Ryu S and Takayanagi T 2006 *Phys. Rev. Lett.* **96** 181602
[60] Lewkowycz A and Maldacena J 2013 *J. High Energy Phys.* **2013** 90
[61] Li K, Han M, Qu D, Huang Z, Long G, Wan Y, Lu D, Zeng B and Laflamme R 2019 *Npj Quantum Inf.* **5** 30
[62] Pastawski F, Yoshida B, Harlow D and Preskill J 2015 *J. High Energy Phys.* **2015** 1
[63] Rovelli C and Smolin L 1995 *Nucl. Phys. B* **442** 593
[64] Rovelli C and Vidotto F 2014 *Covariant loop quantum gravity: an elementary introduction to quantum gravity and spinfoam theory* (Cambridge University Press)
[65] Barbieri A 1998 *Nucl. Phys. B* **518** 714
[66] Li K, Li Y, Han M, Lu S, Zhou J, Ruan D, Long G, Wan Y, Lu D, Zeng B and Laflamme R 2019 *Commun. Phys.* **2** 1
[67] Rovelli C and Speziale S 2006 *Classical Quantum Gravity* **23** 5861
[68] Engle J, Livine E, Pereira R and Rovelli C 2008 *Nucl. Phys. B* **799** 136
[69] Ma X, Jackson T, Zhou H, Chen J, Lu D, Mazurek M D, Fisher K A, Peng X, Kribs D, Resch K J, Ji Z, Zeng B and Laflamme R 2016 *Phys. Rev. A* **93** 032140
[70] Lu D, Xin T, Yu N, Ji Z, Chen J, Long G, Baugh J, Peng X, Zeng B and Laflamme R 2016 *Phys. Rev. Lett.* **116** 230501
[71] Wang H, Zheng W, Yu N, Li K, Lu D, Xin T, Li C, Ji Z, Kribs D, Zeng B, Peng X and Du J 2016 *Sci. China, Ser. A: Math. Phys. Astron.* **59** 100313

[72] Xin T, Lu D, Klassen J, Yu N, Ji Z, Chen J, Ma X, Long G, Zeng B and Laflamme R 2017 *Phys. Rev. Lett.* **118** 020401
[73] Xin T, Lu S, Cao N, Anikeeva G, Lu D, Li J, Long G and Zeng B 2019 *Npj Quantum Inf.* **5** 109
[74] Lu D, Zhu J, Zou P, Peng X, Yu Y, Zhang S, Chen Q and Du J 2010 *Phys. Rev. A* **81** 022308
[75] Xu N, Zhu J, Lu D, Zhou X, Peng X and Du J 2012 *Phys. Rev. Lett.* **108** 130501
[76] Xin T, Wei S, Cui J, Xiao J, Arrazola I, Lamata L, Kong X, Lu D, Solano E and Long G 2020 *Phys. Rev. A* **101** 032307
[77] Li K, Wan Y, Hung L Y, Lan T, Long G, Lu D, Zeng B and Laflamme R 2017 *Phys. Rev. Lett.* **118** 080502
[78] Park A J, McKay E, Lu D and Laflamme R 2016 *New J. Phys.* **18** 043043
[79] Luo Z, You Y Z, Li J, Jian C M, Lu D, Xu C, Zeng B and Laflamme R 2019 *Npj Quantum Inf.* **5** 53
[80] Wei K X, Peng P, Shtanko O, Marvian I, Lloyd S, Ramanathan C and Cappellaro P 2019 *Phys. Rev. Lett.* **123** 090605
[81] Álvarez G A and Suter D 2010 *Phys. Rev. Lett.* **104** 230403
[82] Chen H, Lu D, Chong B, Qin G, Zhou X, Peng X and Du J 2011 *Phys. Rev. Lett.* **106** 180404
[83] Li Z, Liu X, Wang H, Ashhab S, Cui J, Chen H, Peng X and Du J 2019 *Phys. Rev. Lett.* **122** 090504
[84] Wen J W, Qin G Q, Zheng C, Wei S J, Kong X Y, Xin T and Long G L 2020 *Npj Quantum Inf.* **6** 28(2020)
[85] Wang B X, Tao M J, Ai Q, Xin T, Lambert N, Ruan D, Cheng Y C, Nori F, Deng F G, and Long G L 2018 *Npj Quantum Inf.* **4** 52(2018)
[86] Cai J, Retzker A, Jelezko F and Plenio M B 2013 *Nat. Phys.* **9** 168